Research Article | Vol. 30, No. 11 / 23 May 2022 / Optics Express 20063
Optics EXPRESS

Dual-band selective circular dichroism in mid-infrared chiral metasurfaces

HAOTIAN TANG,[1] DANIEL ROSENMANN,[2] DAVID A. CZAPLEWSKI,[2] XIAODONG YANG,[1,4] AND JIE GAO[1,3,5]

[1]Department of Mechanical and Aerospace Engineering, Missouri University of Science and Technology, Rolla, MO 65409, USA
[2]Center for Nanoscale Materials, Argonne National Laboratory, Argonne, IL 60439, USA
[3]Department of Mechanical Engineering, Stony Brook University, Stony Brook, NY 11794, USA
[4]yangxia@mst.edu
[5]jie.gao.5@stonybrook.edu

Abstract: Most chiral metamaterials and metasurfaces are designed to operate in a single wavelength band and with a certain circular dichroism (CD) value. Here, mid-infrared chiral metasurface absorbers with selective CD in dual-wavelength bands are designed and demonstrated. The dual-band CD selectivity and tunability in the chiral metasurface absorbers are enabled by the unique design of a unit cell with two coupled rectangular bars. It is shown that the sign of CD in each wavelength band can be independently controlled and flipped by simply adjusting the geometric parameters, the width and the length, of the vertical rectangular bars. The mechanism of the dual-band CD selection in the chiral metasurface absorber is further revealed by studying the electric field and magnetic field distributions of the antibonding and bonding modes supported in the coupled bars under circularly polarized incident light. Furthermore, the chiral resonance wavelength can be continuously increased by scaling up the geometric parameters of the metasurface unit cell. The demonstrated results will contribute to the advance of future mid-infrared applications such as chiral molecular sensing, thermophotovoltaics, and optical communication.

1. Introduction

Chirality is a particularly important phenomenon in nature which is observed in many substances such as amino acids [1], drug molecules [2], and DNA [3]. A unique feature of a chiral material is the lack of mirror symmetry, in which its chemical structure cannot be superimposed on its mirror image [4], resulting in a different optical absorption when illuminated by left-handed and right-handed circularly polarized (LCP and RCP) light, leading to different circular dichroism (CD) responses [5]. Optical chirality has been widely used in many promising applications such as medical diagnosis [6], pharmaceutical development [7,8], and optical communication [9–11]. However, the optical chirality of natural materials is extremely weak due to the limited chiral light-matter interaction strength, which is caused by the small size of the molecular structure relative to the incident wavelength and the restricted dielectric properties of the material [12]. Recently, optical metamaterials and metasurfaces with specially designed periodic structures have been introduced to offer exceptional functionalities [13–16]. In particular, chiral metamaterials and metasurfaces can be designed to possess strong chiroptical responses by considering various types of asymmetric structures, such as double-bar antennas [17], helices [18,19], split-rings [20,21], letter-shaped patterns [22], and eye-shaped resonators [23]. The enhanced chiroptical responses in chiral metamaterials and metasurfaces can be applied to advance many fields such as CD spectroscopy, photodetection, optical encryption, and perfect absorption [24–29]. However, most of the previously reported chiral metamaterials and metasurfaces operate in a single wavelength band with a certain CD value, where the sign of CD can only be switched by

#457218 https://doi.org/10.1364/OE.457218
Journal © 2022 Received 9 Mar 2022; revised 10 May 2022; accepted 12 May 2022; published 20 May 2022

Optics EXPRESS

alternating the enantiomers. It is important to design chiral metamaterials and metasurfaces in dual- or multiple-wavelength band operation with a controlled CD value in each band. In the mid-infrared wavelength range, in particular, such dual-band operation could offer the benefit of simultaneous detection of multiple featured vibrational fingerprints in chiral molecular sensing [23], and high-efficiency thermophotovoltaics with tailored thermal radiation absorption and emission [30].

In this work, we design and demonstrate mid-infrared chiral metasurface absorbers with selective chiroptical responses in the dual-wavelength bands of 4-5 μm and 5-6 μm based on a three-layer metal-dielectric-metal structure. The dual-band selectivity and tunability of chiral optical absorption under LCP and RCP incident light on the chiral metasurface absorbers are demonstrated by the unique design of two coupled rectangular bars on the top metallic layer. The sign of the CD value in each wavelength band can be independently controlled and switched by simply varying the width and length of the vertical rectangular bar of the unit cell. The underlining mechanism of the dual-band selection of chiral optical absorption in the metasurface is further explained with the simulated electric field and magnetic field distributions of the chiral resonant modes, showing that its physical origin relies on the formation of the antibonding and bonding modes in the two coupled rectangular bars under LCP and RCP incident light. Moreover, the resonance wavelength of the chiral optical absorption can be continuously shifted by scaling up the geometric parameters of the metasurface unit cell. Our strategy in manipulating dual-band selective chiroptical responses of mid-infrared chiral metasurface absorbers provides unprecedented design flexibilities that will impact the advancement of future applications on molecular vibrational sensing, thermophotovoltaics, and optical communication.

2. Design and characterization of dual-band chiral metasurface absorbers

Figure 1(a) shows the schematic of the designed dual-band chiral metasurface absorbers fabricated on a three-layer gold-alumina-gold (Au-Al_2O_3-Au) structure, which is composed of two coupled rectangle bars on the top Au layer of 65 nm thick, the middle Al_2O_3 spacer layer of 250 nm thick, and the bottom Au mirror layer of 200 nm thick on the silicon substrate. The Au layers are deposited using a Lesker PVD250 electron beam evaporator, and the Al_2O_3 layer is deposited in a Lesker CMS18 reactive sputtering system. The top view of the metasurface unit cell is presented in Fig. 1(b), showing the geometric parameters of two coupled rectangular bars with periods of Px and Py. The width and length of the tilted rectangular bar, rotated by an angle α, are A1 and A2, respectively, while the width and length of the vertical rectangular bar are B1 and B2. The tilted rectangular bar in the unit cell breaks the mirror symmetry so that the coupled rectangular bars form a chiral structure producing strong chiroptical responses under the illumination of LCP and RCP light. In addition, since the rectangular bar can provide two plasmonic resonances at different frequencies along its two sides, the chiroptical responses will be displayed in dual-wavelength bands. Moreover, the top and bottom Au layers form a Fabry-Pérot cavity, which allows the incident light to be reflected multiple times to form a resonant mode, further enhancing the chiral optical absorption of incident circularly polarized light. The purpose of the bottom Au mirror layer is to fully block the transmitted light so that the absorption can be obtained easily by the equation $A = 1 - R$, where the A and R represent absorption and reflection, respectively. A focus ion beam (FIB) milling system (FEI Helios Nanolab 600, 30 kV, 92 pA) is used to fabricate the designed dual-band chiral metasurface absorbers. Figure 1(c-f) present the top view of scanning electron microscope (SEM) images of four different chiral metasurface absorbers with the same unit cell periods and the unchanged tilted rectangular bar A, but varying dimensions of the vertical rectangular bar B. The geometric parameters of these metasurface structures are Px = 3.8 μm, Py = 2 μm, A1 = 0.96 μm, A2 = 1.52 μm, α = 29°, B1 = 0.86, 1.10, 1.10, 0.86 μm, and B2 = 1.44, 1.42, 1.65, 1.63 μm for structures 1, 2, 3 and 4, respectively.

Optics EXPRESS

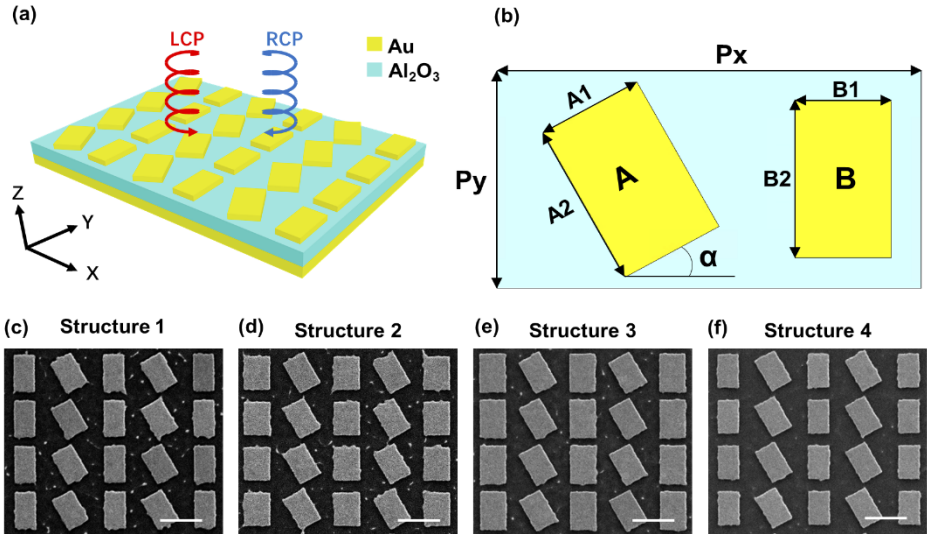

Fig. 1. (a) Schematic of the designed dual-band chiral metasurface absorber. (b) Top view schematic of the metasurface unit cell with two coupled rectangle bars. (c-f) SEM images of the fabricated chiral metasurface absorbers with four different structures having the geometric parameters of Px = 3.8 μm, Py = 2 μm, A1 = 0.96 μm, A2 = 1.52 μm, α = 29°, and for structures 1, 2, 3 and 4, B1 = 0.86, 1.10, 1.10, 0.86 μm, and B2 = 1.44, 1.42, 1.65, 1.63 μm, respectively. Scale bar: 2 μm.

The four metasurface structures are characterized by measuring the chiral optical absorption responses under circular polarizations in the dual-wavelength bands of 4-5 μm and 5-6 μm. The reflection spectra of the four structures are measured by a Fourier transform infrared spectrometer (FTIR, Nicolet 6700) connected to an infrared microscope. The incident LCP and RCP light is obtained by the combination of a linear polarizer and a quarter-wave plate. In addition, the CST Studio Suite software is used to simulate the optical responses of the designed chiral metasurface absorbers under both circular polarizations, where the permittivity of alumina is taken from experimental data [31], and the permittivity of gold is described by the Drude model $\varepsilon_{Au} = \varepsilon_\infty - \omega_p{}^2/(\omega^2 + i\gamma_p\omega)$, where the background dielectric constant $\varepsilon_\infty = 1$, the plasma frequency $\omega_p = 1.37 \times 10^{16}$ rad/s, and the damping constant $\gamma_p = 4.08 \times 10^{13}$ rad/s. The damping constant of the gold film is set to be three times that of bulk gold in the simulation in order to match the experimental results [32]. The measured and simulated absorption spectra for the four metasurface structures with different geometric parameters of the vertical rectangular bar B are depicted in Fig. 2(a-h), showing distinct chiroptical responses in the dual-wavelength bands of 4-5 μm and 5-6 μm for incident LCP and RCP light. Figure 2(a) demonstrates that the two chiral plasmonic resonances of Structure 1 (B1 = 0.86 μm and B2 = 1.44 μm) located in both 4-5 μm and 5-6 μm bands exhibit a stronger absorption of RCP light than that of LCP light. By increasing B1 to 1.10 μm and keeping B2 almost unchanged as 1.42 μm, Structure 2 now displays the opposite chiral absorption responses in the two wavelength bands, where the absorption of LCP light in the 4-5 μm band is stronger than that of RCP light but weaker in the 5-6 μm band, as shown in Fig. 2(b). Next, for Structure 3 where B1 is kept as 1.10 μm and B2 is increased to 1.65 μm, it is observed that the absorption of LCP light is stronger than that of RCP light in both wavelength bands, as shown in Fig. 2(c). Finally, in Structure 4 where B1 is changed back to 0.86 μm and B2 is almost the same, set at 1.63 μm, the opposite chiral absorption responses in the two bands are obtained again, however, now the absorption of RCP light in the 4-5 μm band is stronger than that of LCP light but weaker in the 5-6 μm band, as indicated in Fig. 2(d). The

Optics EXPRESS

slight deviations between the measured and simulated absorption spectra are thought to be due to the defects and roughness of the fabricated rectangular bar patterns introduced during the FIB milling process. It is clear that by adjusting the geometrical parameters, width and length, of the vertical rectangular bar B, the dual-band selectivity and tunability of the chiral optical absorption under LCP and RCP light can be achieved in the designed chiral metasurface absorbers, which is enabled by the unique design of two coupled rectangular bars.

The physical origin of the observed dual-band selection of chiral optical absorption in these four metasurface structures is related to the plasmonic dipolar resonant modes in the two coupled rectangular bars. To understand the underlining mechanism, Fig. 3 displays the simulated electric field distributions across the plane of the upper surface of the Al_2O_3 spacer layer for both LCP and RCP light at the plasmonic resonance wavelengths for chiral absorption. As shown in Fig. 3(a), two plasmonic resonant modes at different wavelengths are formed in the coupled rectangular bars of Structure 1 under the circularly polarized incident light, with the electric fields concentrated on the long and short sides of the two rectangular bars, respectively. It shows that the RCP incident light is strongly coupled into the plasmonic dipolar resonant modes of two rectangular bars in the dual-wavelength bands of 4-5 μm and 5-6 μm, which gives stronger optical absorption than the LCP light. For Structure 2, Fig. 3(b) shows that when the width of the rectangular bar B is increased and becomes larger than that of the rectangular bar A (B1 > A1) while the length B2 stays almost unchanged, the electric field concentration on the long sides of the two bars under LCP illumination is stronger than that under RCP in the 4-5μm band. The electric field distributions in the 5-6 μm band is still similar to that shown in Fig. 3(a), with stronger electric field excitation under RCP illumination. This is because the increased B1 changes the coupling strength of the plasmonic dipolar modes concentrated on the long sides of the two rectangular bars, whereas the dipolar modes located at the short sides are not affected. Then for Structure 3 shown in Fig. 3(c), both the width and length of the rectangular bar B are larger than those of the rectangular bar A (B1 > A1, B2 > A2), so the coupling of the plasmonic dipolar modes accumulated on both the long and short sides are changed compared to that observed in Structure 1. Contrary to Fig. 3(a), it results in a weaker absorption under RCP incidence than that under LCP incidence in both wavelength bands. Finally, for Structure 4 only the length of the rectangular bar B is greater than that of the rectangular bar A (B2 > A2), the coupling of the plasmonic dipolar modes located at the short sides of the two rectangular bars is changed, leading to a stronger absorption in the 5-6 μm band but a weaker absorption in the 4-5μm band for LCP light compared to the RCP case, which exhibits the opposite chiroptical responses obtained for Structure 2. In the two coupled rectangular bars, the tilted rectangular bar A enables symmetry-breaking, which results in strong optical chirality, while the selection and switching of chiral optical absorption in the two wavelength bands are achieved by simply varying the width and length of the vertical rectangular bar B. Moreover, since the electric field excited by the circularly polarized light is concentrated on the long and short sides of the rectangular bars, the chiral resonance wavelengths of the designed metasurface can be easily tuned by changing the dimensions of the rectangular bars.

To further understand the chiral plasmonic modes supported in the designed structures and interpret the design tunability of chiral responses, Fig. 4 and Fig. 5 present the simulated distributions of electric field E_z component, electric field vector and magnetic field vector in the structures. Figure 4 depicts the distributions of E_z component at the interface between the top Au layer and the dielectric spacer for LCP and RCP excitation at the two wavelength bands in all four structures. The E_z distributions indicate the charge density profiles, and the simplified mode sketches with the corresponding charge distributions are plotted in Table 1 to summarize the characteristic plasmonic modes (modes a, b, c and d) in the two coupled rectangular bars. The strong near-field coupling between the two bars via the adjacent bar corners produces the antibonding mode with higher energy and the bonding mode with lower energy. The antibonding

Optics EXPRESS

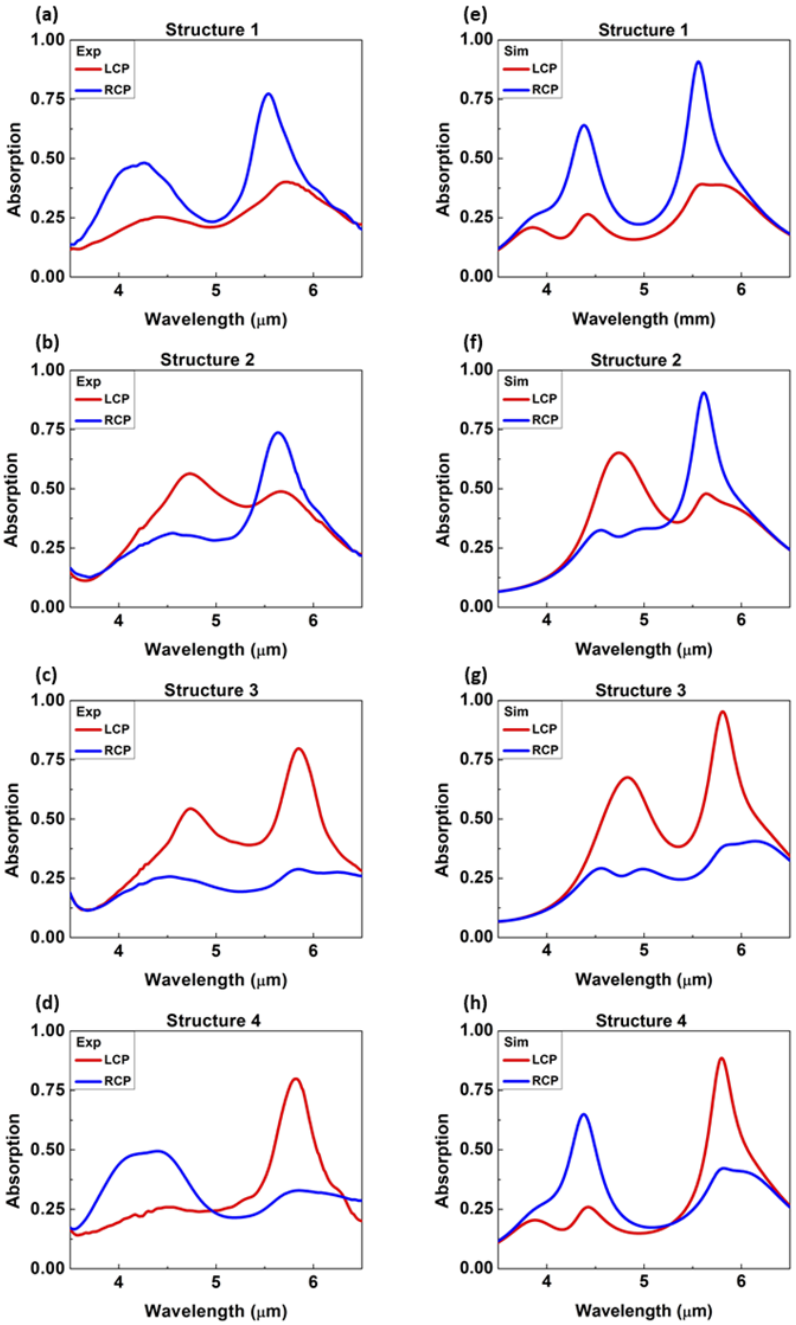

Fig. 2. (a-d) Measured and (e-h) simulated optical absorption spectra for the designed dual-band chiral metasurface structures with different geometric parameters.

Optics EXPRESS

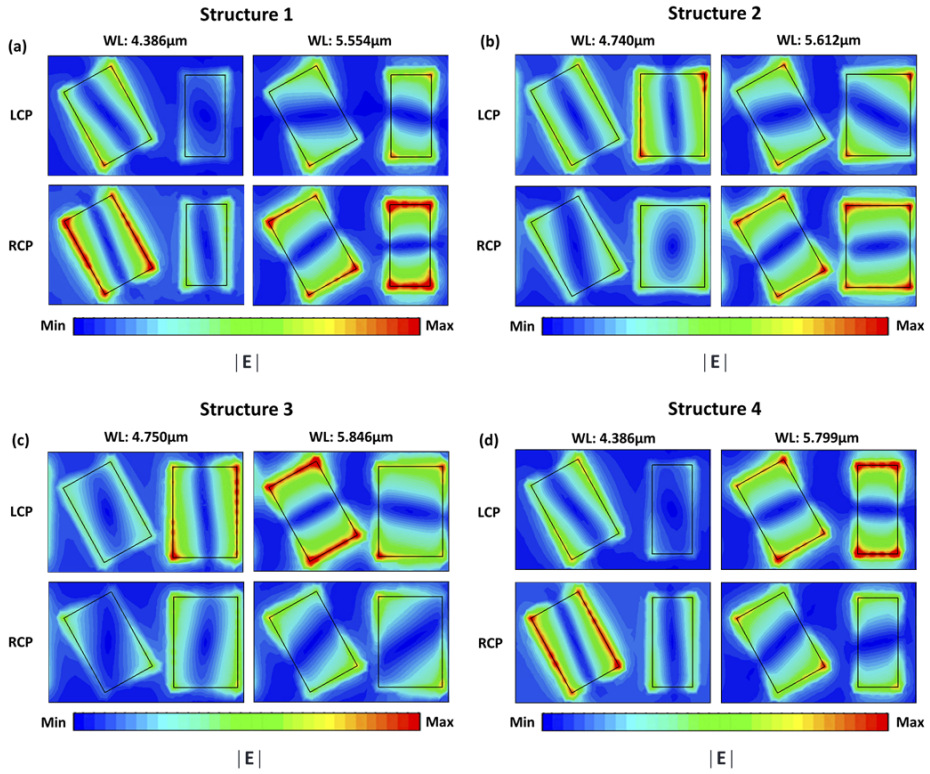

Fig. 3. (a-d) Simulated electric field distributions in Structures 1-4 at the interface between the top Au layer and the dielectric spacer under LCP and RCP incidence at the two chiral resonance wavelengths (WL) in the 4-5 μm and 5-6 μm bands.

mode (illustrated as mode a in Table 1) is formed by the accumulation of charges of the same sign at the adjacent bar corners, while the bonding mode (illustrated as mode b in Table 1) is created with the opposite charges located at the adjacent corners. For example, in Structure 4, mode a is displayed in the bottom-left picture and mode b is shown in the top-right picture of Fig. 4(d). It is noteworthy that the charges are located along the long sides of two bars in the antibonding mode at the shorter wavelength λ_1, whereas the charges are distributed along the short sides of the bars at the longer wavelength λ_2. On the contrary, there are two weakly-coupled modes appeared in the top-left picture and the bottom-right picture of Fig. 4(d) (illustrated as mode c and mode d in Table 1). Mode c is excited by the LCP incident light where the charge is localized at the bottom-left corners of two bars, whereas mode d is coupled by the RCP light with the charge concentrated at the bottom-right corners of both bars, so the optical coupling between the two bars is extremely weak. Figure 5(a) plots the spatial distributions of electric field vector at the middle plane of the top Au layer in Structure 4, and Fig. 5(b) shows the spatial distributions of magnetic field vector at the middle plane of the dielectric spacer layer. The orientations of electric dipoles (p_A and p_B) and magnetic dipoles (m_A and m_B) in individual bars are marked for visualization. In the configurations of mode a and mode b, the direct interplay of non-orthogonal electric dipoles and magnetic dipoles results in the intrinsic chirality polarizability of the two coupled rectangular bars, and thus both the antibonding and bonding plasmonic modes exhibit strong chiral absorption. On the other hand, the chirality polarizability induced from the non-orthogonal electric and magnetic dipoles is relatively weak, so mode c and mode d present a low chiral absorption.

Optics EXPRESS

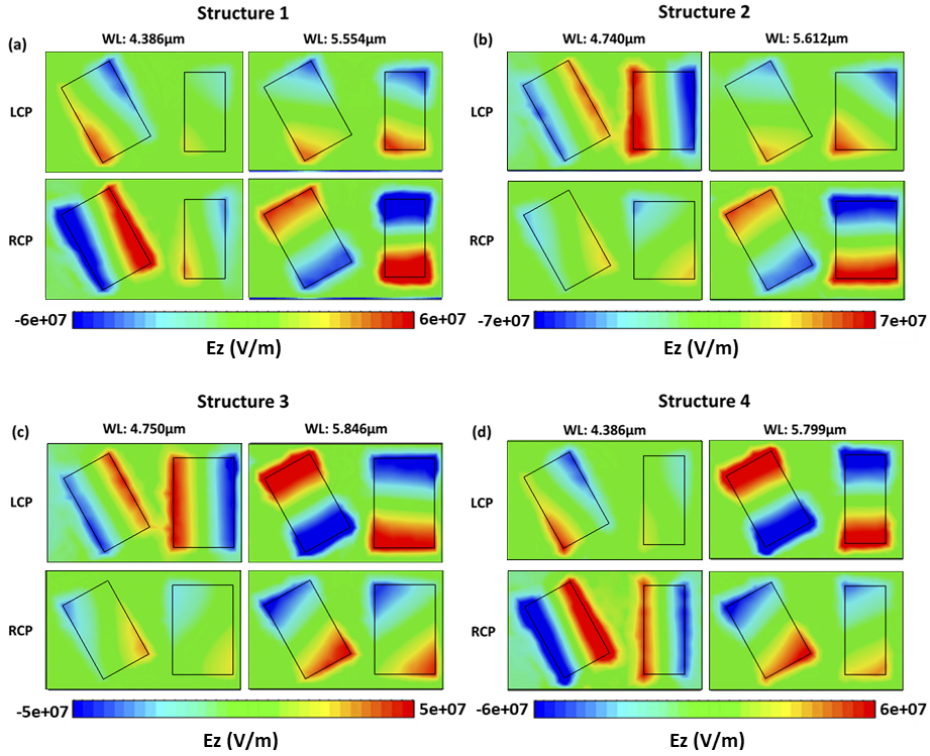

Fig. 4. (a-d) Simulated electric field distributions of E_z component in Structures 1-4 at the interface between the top Au layer and the dielectric spacer for LCP and RCP excitation at the two chiral resonance wavelengths (WL) in the 4-5 μm and 5-6 μm bands.

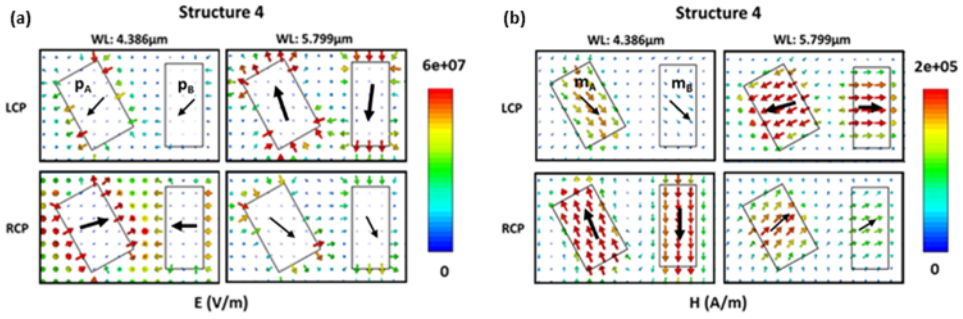

Fig. 5. (a) Simulated electric field vector distributions at the middle plane of the top Au layer and (b) simulated magnetic field vector distributions at the middle plane of the dielectric spacer layer in Structure 4. The orientations of electric dipoles (p_A and p_B) and magnetic dipoles (m_A and m_B) in individual bars are marked for visualization.

Optics EXPRESS

Table 1. Mode sketches with the corresponding charge distributions for modes a, b, c, d in Structures 1-4.

	mode a	mode b	mode c	mode d
	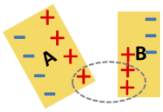	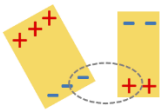	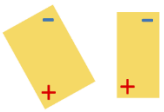	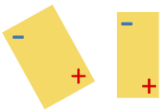
Structure 1	RCP, bar A, λ_1	RCP, bar B, λ_2	LCP, bar A, λ_1 LCP, bar B, λ_2	--
Structure 2	LCP, bar B, λ_1	RCP, bar B, λ_2	LCP, bar B, λ_2	RCP, bar B, λ_1
Structure 3	LCP, bar B, λ_1	LCP, bar A, λ_2	--	RCP, bar B, λ_1 RCP, bar A, λ_2
Structure 4	RCP, bar A, λ_1	LCP, bar A, λ_2	LCP, bar A, λ_1	RCP, bar A, λ_2

Moreover, the selection of chiral excitations for mode a and mode b is discussed as follows. For the antibonding mode (mode a), the charge distribution in bar A is rotated in anticlockwise direction which follows the electric field rotation of RCP light, whereas the charge in bar B is rotated in clockwise direction following the LCP light. In addition, the bar with a larger width is designed to be majorly excited by the incident light at λ_1 and then couples to the other bar to form the plasmonic resonant mode. As a result, in Structure 1 and Structure 4, bar A with the larger width is strongly excited with RCP light (labeled in Table 1 as "RCP, bar A, λ_1") and then couples to bar B, leading to a high absorption for the antibonding mode (mode a) under RCP illumination. Instead, in Structure 2 and Structure 3, bar B with the larger width is favorably excited under LCP incidence (labeled in Table 1 as "LCP, bar B, λ_1") and couples to bar A, thus a high absorption under LCP illumination is observed. For the bonding mode (mode b), the charge rotation directions in bar A and bar B are flipped compared to the antibonding mode, which corresponds to the rotation directions of the LCP and RCP incident light, respectively. Here, the bar with a smaller length is designed to be strongly excited by the incident light at λ_2 and then couples to the other bar. Therefore, in Structure 1 and Structure 2, bar B with the smaller length is excited with RCP light (labeled in Table 1 as "RCP, bar B, λ_2"), giving a high absorption for the bonding mode (mode b) under RCP illumination. On the contrary, in Structure 3 and Structure 4, bar A with the smaller length is excited with LCP light (labeled in Table 1 as "LCP, bar A, λ_2") to achieve a high absorption under LCP illumination.

The CD in absorption is defined as $\mathrm{CD} = A_{LCP} - A_{RCP}$, giving a positive CD value when the absorption of LCP light is greater than that of RCP light, and negative otherwise. Based on Fig. 2, the measured and simulated CD spectra of the four metasurface structures are plotted in Fig. 6(a,b). A significant advantage of the designed dual-band chiral metasurface absorber is that the sign of the CD value in each wavelength band of 4-5 μm and 5-6 μm can be independently selected and controlled by only varying the dimensions of B1 and B2 in the vertical rectangular bar B. It is shown that the sign of CD is negative in both wavelength bands for Structure 1. As only B1 > A1 in Structure 2, the CD value at 4-5 μm flips into positive, but the CD remains negative at 5-6 μm because B2 is almost unchanged. Next, as both B1 > A1 and B2 > A2 in Structure 3, the CD values are switched from negative to positive in both bands compared to those obtained for Structure 1. With only B2 > A2 in Structure 4, the CD value at the 5-6 μm band is flipped from negative to positive compared with Structure 1, but the CD stays negative for the 4-5 μm band. These results indicate that the CD flipping in the wavelength band of 4-5 μm can be obtained by simply varying B1, while the CD flipping in the band of 5-6 μm can be achieved by adjusting B2, making it possible to independently control the value of CD in each band. Furthermore, the simulated CD spectrum mapping for Structure 1 as a function of the geometrical parameter B1 as it increases from 0.8 to 1.2 μm is displayed in Fig. 6(c). The

Optics EXPRESS

transition point in which CD flips sign from negative to positive is observed for B1 = 0.98 μm in the 4-5 μm band. Figure 7(a,b) display the simulated absorption spectra and electric field distributions for such structure at the CD transition point. It is indicated that the absorption values in the 4-5 μm band under LCP and RCP light are almost the same, and the antibonding mode (mode a) is excited in the coupled rectangular bars for both LCP and RCP illumination, leading to the zero CD value. The CD spectrum mapping for Structure 2 with B2 varying from 1.4 to 1.8 μm is also plotted in Fig. 6(d). The switching of CD from negative to positive is achieved at approximately B2 = 1.55 μm for the 5-6 μm band. Figure 7(c) plots the simulated absorption spectra of the structure at the CD switching point under LCP and RCP illumination, showing that the structure absorbs both LCP and RCP incident light almost equivalently and exhibits the zero CD. The electric field distributions shown in Fig. 7(d) further suggest that the bonding mode (mode b) is excited in the couped rectangular bars with both LCP and RCP light. It is therefore shown that by simply varying the dimension of the geometric parameters B1 and B2, the sign and the magnitude of CD can be selected and manipulated in the two wavelength bands.

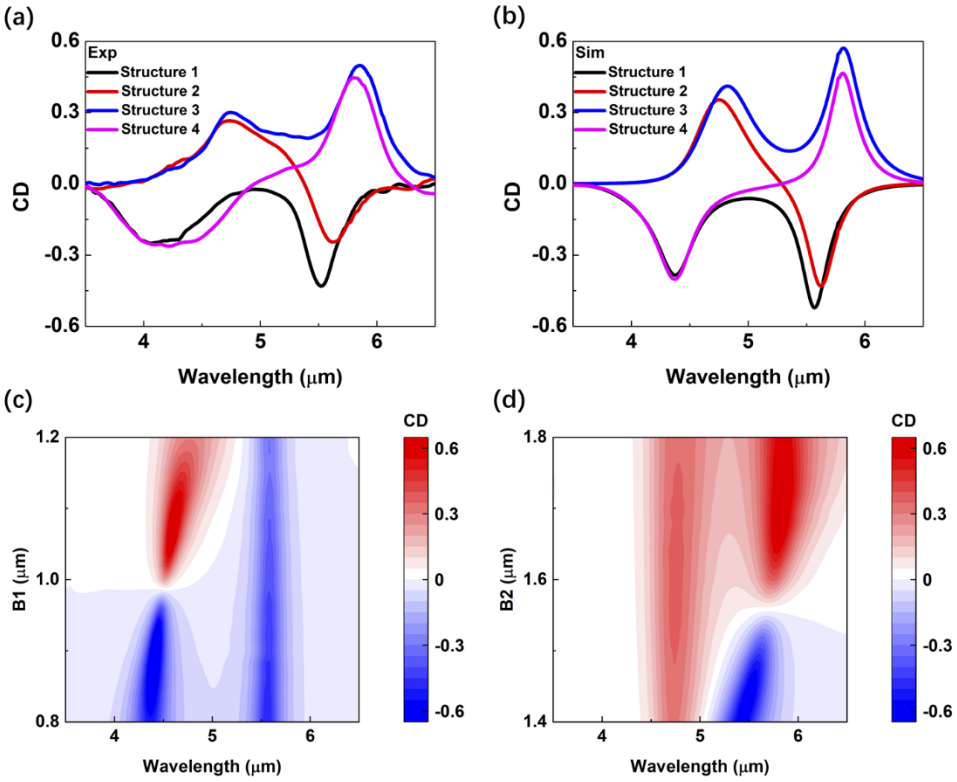

Fig. 6. (a) Measured and (b) simulated CD spectra of four metasurface structures. (c) Simulated CD spectrum mapping for Structure 1 as a function of the value of the geometric parameter B1. (d) Simulated CD spectrum mapping for Structure 2 obtained by varying B2.

In addition, the resonance wavelength of the chiral absorption can be continuously shifted by scaling up the geometric parameters of the metasurface unit cell. The scale-up factor of k^n is applied to all the geometric parameters of the unit cell except the rotation angle α, while keeping the thicknesses of the metal and dielectric layers unchanged. The scaling constant has a value of $k = 1.03$ and the exponent $n = 0$, 1, 2, 3 and 4. By considering Structure 1 as one example, Fig. 8(a,b) plot the measured and simulated optical absorption spectra of the chiral metasurface absorbers with different scale-up factors under LCP and RCP incidence, with the corresponding

Optics EXPRESS

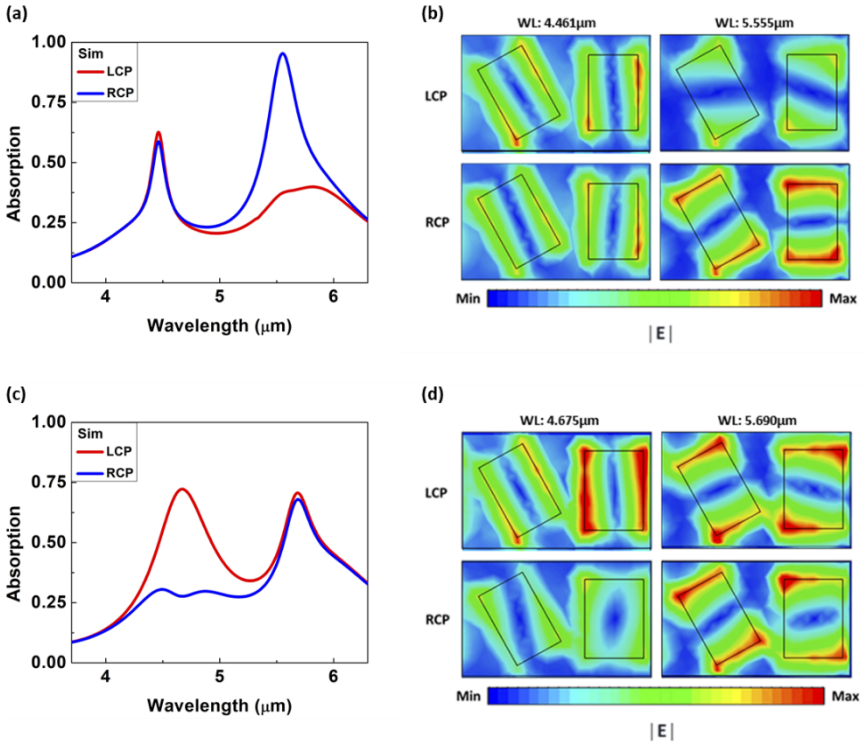

Fig. 7. Simulated absorption spectra and electric field distributions for the structures at the CD transition point. (a, b) Structure with B1 = 0.98 μm for achieving zero CD in the 4-5 μm band. (c, d) Structure with B2 = 1.55 μm for obtaining zero CD in the 5-6 μm band.

CD spectra shown in Fig. 8(c,d). It shows that as the metasurface unit cell is scaled up to a larger size, the plasmonic resonance wavelength is continuously increased, while the absorption of RCP light is always stronger than that of LCP light and thus the value of CD remains negative in both wavelength bands.

Optics EXPRESS

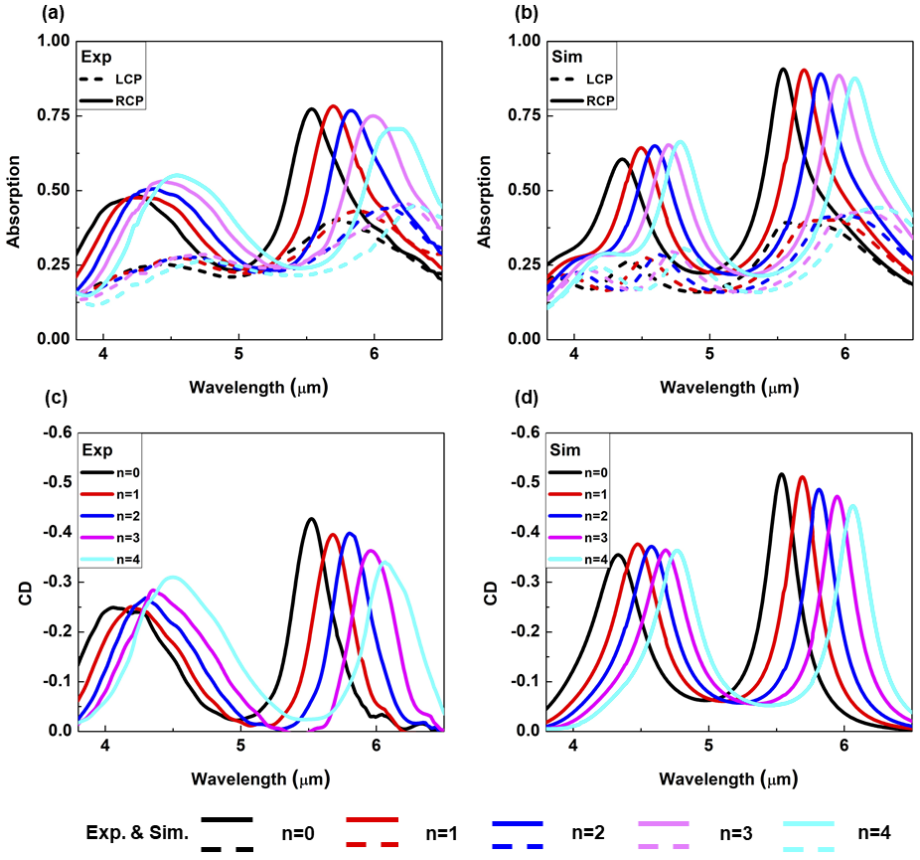

Fig. 8. (a) Measured and (b) simulated optical absorption spectra for Structure 1 with different scale-up factors k^n. (c) Measured and (d) simulated CD spectra corresponding to (a) and (b).

3. Conclusion

In summary, mid-infrared chiral metasurface absorbers with selective chiral optical absorption in dual-wavelength bands have been designed and demonstrated. The dual-band CD selectivity and tunability under LCP and RCP incident light in the chiral metasurface absorbers is enabled by the unique design of two coupled rectangular bars on the top metallic layer. It is demonstrated that the sign of CD in each wavelength band can be independently controlled and flipped through the modification of the interactions between the two rectangular bars, which is achieved by simply varying the value of the geometric parameters, width and length, of the vertical rectangular bar. The mechanism of the dual-band chiroptical response and CD selection in the designed chiral metasurface is revealed by analyzing the simulated electric field and magnetic field distributions of the antibonding and bonding modes formed in the two coupled rectangular bars under both LCP and RCP incidence. In addition, the resonance wavelength of the chiral optical absorption is continuously tuned by scaling up the geometric parameters of the metasurface unit cell. Our current results show the design tunability of metasurface structures to achieve different chiral optical responses by slightly adjusting the geometric parameters. In the future, dynamically tuning of the chiroptical properties in metasurfaces using phase change materials, electrical gating and strain tuning mechanisms can be implemented. The ability to control the dual-band selective CD in mid-infrared chiral metasurface absorbers will open further opportunities for many applications

Optics EXPRESS

such as thermal energy harvesting, optical communication, circular polarization photodetection, chiral sensing and imaging [33–35]. We envision the demonstrated dual-band chiral metasurfaces will create a promising chiral sensing platform for selective and sensitive detection of chiral molecules, especially for the mid-infrared vibrational sensing of phonon modes.

Funding. National Science Foundation (DMR-1552871, ECCS-1653032); U.S. Department of Energy (DE-AC02-06CH11357).

Acknowledgments. This work was performed, in part, at the Center for Nanoscale Materials, a U.S. Department of Energy Office of Science User Facility, and supported by the U.S. Department of Energy, Office of Science, under Contract No. DE-AC02-06CH11357. The authors acknowledge the support from the Intelligent Systems Center and the facility support from the Materials Research Center at Missouri S&T.

Disclosures. The authors declare no conflicts of interest.

Data availability. Data underlying the results presented in this paper are not publicly available at this time but may be obtained from the authors upon reasonable request.

References

1. R. M. Hazen and D. S. Sholl, "Chiral selection on inorganic crystalline surfaces," Nat. Mater. **2**(6), 367–374 (2003).
2. Z. L. Wu, Y. R. Liu, E. H. Hill, and Y. B. Zheng, "Chiral metamaterials via moiré stacking," Nanoscale **10**(38), 18096–18112 (2018).
3. Y. Liu, J. Xiao, J. Koo, and B. Yan, "Chirality-driven topological electronic structure of DNA-like materials," Nat. Mater. **20**(5), 638–644 (2021).
4. B. Semnani, J. Flannery, R. Al Maruf, and M. Bajcsy, "Spin-preserving chiral photonic crystal mirror," Light: Sci. Appl. **9**(1), 23 (2020).
5. Y. J. Huang, X. Xie, M. B. Pu, Y. H. Guo, M. F. Xu, X. L. Ma, X. Li, and X. G. Luo, "Dual-Functional Metasurface toward Giant Linear and Circular Dichroism," Adv. Opt. Mater. **8**(11), 1902061 (2020).
6. T. A. Keiderling, "Structure of Condensed Phase Peptides: Insights from Vibrational Circular Dichroism and Raman Optical Activity Techniques," Chem. Rev. **120**(7), 3381–3419 (2020).
7. E. Francotte, W. Lindner, R. Mannhold, H. Kubinyi, and G. Folkers, *Chirality in drug research* (Wiley-VCH Weinheim, 2006).
8. I. K. Reddy and R. Mehvar, *Chirality in drug design and development* (CRC Press, 2004).
9. Y. Chen, J. Gao, and X. Yang, "Direction-Controlled Bifunctional Metasurface Polarizers," Laser Photonics Rev. **12**(12), 1800198 (2018).
10. R. Farshchi, M. Ramsteiner, J. Herfort, A. Tahraoui, and H. T. Grahn, "Optical communication of spin information between light emitting diodes," Appl. Phys. Lett. **98**(16), 162508 (2011).
11. W. Li, Z. J. Coppens, L. V. Besteiro, W. Wang, A. O. Govorov, and J. Valentine, "Circularly polarized light detection with hot electrons in chiral plasmonic metamaterials," Nat. Commun. **6**(1), 8379 (2015).
12. S. Yoo and Q. H. Park, "Metamaterials and chiral sensing: a review of fundamentals and applications," Nanophotonics **8**(2), 249–261 (2019).
13. Y. Chen, J. Gao, and X. Yang, "Chiral grayscale imaging with plasmonic metasurfaces of stepped nanoapertures," Adv. Opt. Mater. **7**(6), 1801467 (2019).
14. L. Li, W. Wang, T. S. Luk, X. Yang, and J. Gao, "Enhanced quantum dot spontaneous emission with multilayer metamaterial nanostructures," ACS Photonics **4**(3), 501–508 (2017).
15. D. R. Smith, W. J. Padilla, D. C. Vier, S. C. Nemat-Nasser, and S. Schultz, "A composite medium with simultaneously negative permeability and permitivity," Phys. Rev. Lett. **84**(18), 4184–4187 (2000).
16. N. Yu and F. Capasso, "Flat optics with designer metasurfaces," Nat. Mater. **13**(2), 139–150 (2014).
17. L. Ouyang, W. Wang, D. Rosenmann, D. A. Czaplewski, J. Gao, and X. Yang, "Near-infrared chiral plasmonic metasurface absorbers," Opt. Express **26**(24), 31484–31489 (2018).
18. M. Esposito, V. Tasco, M. Cuscunà, F. Todisco, A. Benedetti, I. Tarantini, M. D. Giorgi, D. Sanvitto, and A. Passaseo, "Nanoscale 3D chiral plasmonic helices with circular dichroism at visible frequencies," ACS Photonics **2**(1), 105–114 (2015).
19. J. K. Gansel, M. Thiel, M. S. Rill, M. Decker, K. Bade, V. Saile, G. V. Freymann, S. Linden, and M. Wegener, "Gold helix photonic metamaterial as broadband circular polarizer," Science **325**(5947), 1513–1515 (2009).
20. M. Decker, R. Zhao, C. M. Soukoulis, S. Linden, and M. Wegener, "Twisted split-ring-resonator photonic metamaterial with huge optical activity," Opt. Lett. **35**(10), 1593–1595 (2010).
21. L. Kang, C. Wang, X. Guo, X. Ni, Z. Liu, and D. H. Werner, "Nonlinear chiral meta-mirrors: enabling technology for ultrafast switching of light polarization," Nano Lett. **20**(3), 2047–2055 (2020).
22. M. S. Mahmud, D. Rosenmann, D. A. Czaplewski, J. Gao, and X. Yang, "Chiral plasmonic metasurface absorbers in the mid-infrared wavelength range," Opt. Lett. **45**(19), 5372–5375 (2020).
23. M. S. Mahmud, D. Rosenmann, D. A. Czaplewski, J. Gao, and X. Yang, "Plasmon-phonon coupling between mid-infrared chiral metasurfaces and molecular vibrations," Opt. Express **28**(14), 21192–21201 (2020).

Optics EXPRESS

24. A. Y. Zhu, W. T. Chen, A. Zaidi, Y.-W. Huang, M. Khorasaninejad, V. Sanjeev, C.-W. Qiu, and F. Capasso, "Giant intrinsic chiro-optical activity in planar dielectric nanostructures," Light: Sci. Appl. **7**(2), 17158 (2018).
25. S. T. Siday, P. P. Vabishchevich, L. Hale, C. T. Harris, T. S. Luk, J. L. Reno, I. Brener, and O. Mitrofanov, "Terahertz Detection with Perfectly-Absorbing Photoconductive Metasurface," Nano Lett. **19**(5), 2888–2896 (2019).
26. Y. Chen, X. Yang, and J. Gao, "3D Janus plasmonic helical nanoapertures for polarization-encrypted data storage," Light: Sci. Appl. **8**(1), 45 (2019).
27. G. Y. Qu, W. H. Yang, Q. H. Song, Y. L. Liu, C. W. Qiu, J. C. Han, D. P. Tsai, and S. M. Xiao, "Reprogrammable meta-hologram for optical encryption," Nat. Commun. **11**(1), 5484 (2020).
28. G. M. Akselrod, J. Huang, T. B. Hoang, P. T. Bowen, L. Su, D. R. Smith, and M. H. Mikkelsen, "Large-area metasurface perfect absorbers from visible to near-infrared," Adv. Mater. **27**(48), 8028–8034 (2015).
29. L. Ouyang, D. Rosenmann, D. A. Czaplewski, J. Gao, and X. Yang, "Broadband infrared circular dichroism in chiral metasurface absorbers," Nanotechnology **31**(29), 295203 (2020).
30. H. Deng, T. Wang, J. Gao, X. Yang, D. Huixu, W. Tianchen, G. Jie, and Y. Xiaodong, "Metamaterial thermal emitters based on nanowire cavities for high-efficiency thermophotovoltaics," J. Opt. **16**(3), 035102 (2014).
31. J. Kischkat, S. Peters, B. Gruska, M. Semtsiv, M. Chashnikova, M. Klinkmüller, O. Fedosenko, S. Machulik, A. Aleksandrova, G. Monastyrskyi, Y. Flores, and W. Ted Masselink, "Mid-infrared optical properties of thin films of aluminum oxide, titanium dioxide, silicon dioxide, aluminum nitride, and silicon nitride," Appl. Opt. **51**(28), 6789–6798 (2012).
32. W. Wan, X. Yang, and J. Gao, "Strong coupling between mid-infrared localized plasmons and phonons," Opt. Express **24**(11), 12367–12374 (2016).
33. Y. Chen, C. Zhao, Y. Z. Zhang, and C. W. Qiu, "Integrated Molar Chiral Sensing Based on High-Q Metasurface," Nano Lett. **20**(12), 8696–8703 (2020).
34. H. Kurebayashi, J. H. Garcia, S. Khan, J. Sinova, and S. Roche, "Magnetism, symmetry and spin transport in van der Waals layered systems," Nat. Rev. Phys. **4**(3), 150–166 (2022).
35. E. Ashalley, C.-P. Ma, Y.-S. Zhu, H.-X. Xu, P. Yu, and Z.-M. Wang, "Recent progress in chiral absorptive metamaterials," J. Electron. Sci. Technol. **19**(3), 100098 (2021).